The Astrophysical Journal, 929:11 (12pp), 2022 April 10 https://doi.org/10.3847/1538-4357/ac5909

On the Variation in the Volumetric Evolution of CMEs from the Inner to Outer Corona

Satabdwa Majumdar[1], Ritesh Patel[1,2], and Vaibhav Pant[2]
[1] Indian Institute of Astrophysics, 2nd Block, Koramangala, Bangalore, 560034, India
[2] Aryabhatta Research Institute of Observational Sciences, Nainital, 263001, India
Received 2021 November 2; revised 2022 February 23; accepted 2022 February 23; published 2022 April 8

Abstract

Some of the major challenges faced in understanding the early evolution of coronal mass ejections (CMEs) are due to the limited observations in the inner corona ($<3\ R_{\odot}$) and the plane-of-sky measurements. In this work, we have thus extended the application of the Graduated Cylindrical Shell (GCS) model to inner coronal observations from the ground-based coronagraph K-Cor of the Mauna Loa Solar Observatory, along with the pairs of observations from COR-1 on board the Solar Terrestrial Relations Observatory. We study the rapid initial acceleration and width expansion phases of five CMEs in white light at the lower heights. We also study the evolution of the modeled volumes of these CMEs in the inner corona and report, for the first time, a power-law dependence of CME volume with distance from the Sun. We further find that the volumes of the ellipsoidal leading front and the conical legs follow different power laws, thus indicating differential volume expansion throughout a CME. The study also reveals two distinct power laws for the total volume evolution of CMEs in the inner and outer corona, thus suggesting different expansion mechanisms at these different heights. Besides aiding our current understanding of CME evolution, these results will also provide better constraints to CME initiation and propagation models. Also, given the loss of the STEREO-B (and hence COR-1B data) from 2016, the modified GCS model presented here will still enable stereoscopy in the inner corona for the 3D study of CMEs in white light.

Unified Astronomy Thesaurus concepts: Solar coronal mass ejections (310)

1. Introduction

One of the most fascinating and intriguing phenomena occurring in the Sun's corona are coronal mass ejections (CMEs), which involve large-scale releases of magnetized plasma outward into the heliosphere. They are most generally defined as discrete, bright, white-light features propagating outward in the coronagraph field of view (FOV; Hundhausen et al. 1984). They largely vary in their shapes and appearances, and are known to show a wide range of kinematic properties (for a review, see Webb & Howard 2012). Apart from that, CMEs are also the major drivers of space weather, and the ones traveling toward Earth can have a severe impact on it by creating geomagnetic storms that can pose a threat to our several technological advancements as well as our life as a whole (Gosling 1993; Schwenn et al. 2005). Such a plausible event of chance demands better preparation, and hence, as a prerequisite, a very good understanding of their kinematics.

It is known that CME kinematics is an outcome of the interplay of three forces, namely the Lorentz force, the gravitational force, and the viscous drag force, with the latter arising due to interaction with the ambient solar wind (Webb & Howard 2012). The outcome of this interplay of forces is reflected in a three-phase kinematic profile, with an initial gradual rising phase, followed by an impulsive phase, and then a residual propagation phase (Zhang et al. 2001, 2004). The initial rising phase is marked by a very weakly accelerated motion (Cheng et al. 2020), while the later residual phase is seen as a propagation with an almost constant or decreasing speed (see Gopalswamy et al. 2000). The main impulsive acceleration phase, however, is qualitatively very different from the initial slow rising phase, and involves a rapid increase in acceleration in a short period of time, which shoots the CMEs to high velocities (e.g., Bein et al. 2011; Cheng et al. 2020; Patel et al. 2021). Earlier studies have suggested that this main acceleration phase occurs at the lower coronal heights, and hence it might not always be captured using traditional white-light coronagraphic observations (Gallagher et al. 2003; Temmer et al. 2008; Majumdar et al. 2021a). Earlier attempts at measurements of this main acceleration phase have been reported by several studies in the past. In most of these works, the method either relied on measurements on the plane of the sky, thus introducing discrepancies due to projection effects (e.g., St. Cyr et al. 1999; Zhang & Dere 2006; Balmaceda et al. 2018), or involved combining white light with extreme-ultraviolet (EUV) data to track a CME (e.g., Vršnak et al. 2007; Bein et al. 2011), where it is still debatable whether the same features are observed in emission lines and in white light (see Song et al. 2019). Now, although we have an understanding of the impact of the drag force on the kinematics (Sachdeva et al. 2015, and references therein), the impact of the Lorentz force still eludes clear understanding. Recently, Majumdar et al. (2020) used the Graduated Cylindrical Shell (GCS) model (developed by Thernisien et al. 2006, 2009; Thernisien 2011) to study the 3D evolution of CMEs in the inner and outer corona, and reported that the true height up to which the imprint of the Lorentz force remains dominant lies in the range of 2.5–3 $R_{\odot}$, thus further indicating the importance of inner corona observations.

CMEs, apart from radial propagation, also show lateral expansion of their angular width (see Kay et al. 2015) until a certain critical height, after which they propagate with almost constant width (e.g., Moore et al. 2007; Zhao et al. 2010). The usual method of width estimation involves the projected angular span between the position angles of the two extreme flanks of the CME (Zhao et al. 2010), but such estimation

suffers from a lot of projection effects. In this regard, Cremades et al. (2020) used the GCS model to study the axial and lateral width expansion of CMEs by combining white-light and EUV observations. Also, Majumdar et al. (2020), using the GCS model, reported on the observational evidence that the angular width expansion and the impulsive accelerations are just manifestations of the same Lorentz force, as conjectured earlier by Subramanian et al. (2014) and Suryanarayana (2019). In this regard, it was further reported that the evolution and width expansion of CMEs are non-self-similar in the inner corona (Cremades et al. 2020), while they are self-similar in the outer corona (Subramanian et al. 2014). It is also worth noting that the distribution of the angular widths of slow and fast CMEs from different source regions have been known to follow different power-law profiles, thus indicating the possibility of different generation mechanisms (as recently reported by Pant et al. 2021). Thus, a study of the evolution of CME volume (which is influenced by CME width expansion) would shed more light on this aspect of CME evolution. In this regard, Holzknecht et al. (2018) used the GCS model to estimate the volume of a CME. Later, this treatment was also used by Temmer et al. (2021) to study the density evolution of CMEs with distance from the Sun, but both these works reported on results in the outer corona and the heliosphere, and thus we do not have a good understanding of the evolution of total volume in the inner corona.

A major challenge in the understanding of early CME kinematics in the inner corona has been due to limited observational white-light data below 3 $R_\odot$ and projection effects. Several techniques have been developed to address the latter issue (see Mierla et al. 2008; Thernisien et al. 2009; Joshi & Srivastava 2011; Hutton & Morgan 2017), but the implementation of such techniques for the inner corona has been limited. To address these shortcomings, we extend the implementation of the GCS model to the inner corona observations from the ground-based coronagraph K-Cor of the Mauna Loa Solar Observatory (MLSO), which offers an FOV of 1.05–3 $R_\odot$. This will enable us to capture the initial impulsive phase of CMEs uniquely in white-light observations. Using this extended GCS model, we thus study the early 3D evolutions of five CMEs by studying their kinematic profiles, widths, and volume evolutions as they propagate from the inner to the outer corona. We outline the data source and working method in Section 2, followed by our results in Section 3, and we present our main conclusions and discussions in Section 4.

2. Data and Method

2.1. Data Source and Data Preparation

The data used in this work are taken from the coronagraphs COR-1 (FOV of 1.5–4 $R_\odot$) and COR-2 (FOV of 2.5–15 $R_\odot$) and the Extreme UltraViolet Imager (EUVI) of the Sun Earth Connection Coronal and Heliospheric Investigation package (SECCHI; Howard et al. 2002) on board the twin spacecraft Solar Terrestrial Relations Observatory (STEREO; Kaiser et al. 2008); from the K-Cor (DOI: 10.5065/D69G5JV8) ground-based coronagraph (FOV of 1.05–3 $R_\odot$) of MLSO; and from the Large Angle Spectroscopic Coronagraph (LASCO; Brueckner et al. 1995; FOV of 2.2–30 $R_\odot$). The level 0.5 data of EUVI, COR-1, and COR-2 were reduced to level 1.0, using the *secchi_prep.pro* routine in IDL. For the K-Cor data, we used the 2 min cadence level 2.0 data processed through the Normalized Radially Graded Filter (Morgan et al. 2006, 2012), and for LASCO, we used level 1 data (corrected for instrumental effects and solar north, and calibrated to physical units of brightness). Finally, base difference images were created for K-Cor, COR-1, COR-2, and LASCO by subtracting a pre-event image from successive images of the event thereafter.

2.2. Event Selection

Since this work involves combining data from the COR-1 and COR-2 coronagraphs on STEREO, the LASCO coronagraphs (FOV of 1.5–4 $R_\odot$) on SOHO, and the K-Cor of MLSO, only those events could be selected that were simultaneously observed by these instruments. It should be noted here that K-Cor and LASCO are not simultaneously used by the GCS model, but rather LASCO is replaced by K-Cor for the lower coronal heights. Now, K-Cor being a ground-based coronagraph, only the daytime observations are available (from approximately 17:30 UT to 02:30 UT), and this largely restricted the event selection. Also, those CMEs were selected that had a distinct leading edge in the FOVs of the above coronagraphs, thus assuring unambiguous tracking in the successive frames. Since K-Cor views the solar corona through the Earth's atmosphere, the data is affected by weather conditions. Also, the identified CMEs tend to be fainter in K-Cor as compared to COR-1, thus rendering tracking more challenging. This could be due to the bright sky background leading to a low signal or to the fact that CMEs tend to gather mass at these low heights (Thompson et al. 2017). Based on the above criteria, five CMEs were selected from the K-Cor catalog, which occurred between 2014 February and 2016 January.

2.3. The GCS Fitting to STEREO and K-Cor Data

The GCS model was developed to fit a synthetic flux rope to a pair of coronagraph images taken from the two different vantage points offered by the positions of STEREO-A/B. A provision is also made for including observations from the LASCO coronagraphs as a third vantage point. In this work, to study the evolution of CMEs from the inner corona, we first extended the model further, to include observations of the inner corona from the K-Cor of MLSO as a third vantage point (along the Sun–Earth line), as the FOV of K-Cor will largely aid in understanding the early evolutions of CMEs. Since the header structure of the K-Cor data is different than that of the LASCO data, the primary codes that generate the synthetic flux rope, namely *rtsccguicloud.pro* and *rtcloud.pro*, needed to be modified. Hence, a similar block of code (as was present for LASCO) was developed for the K-Cor observations, by introducing relevant keywords for the K-Cor data corresponding to the keywords for the LASCO data relating to the above procedures. This was added with a condition that, simultaneously, either K-Cor or LASCO observations are to be present along with the STEREO observations. Thanks to the overlapping FOVs, the K-Cor observations were combined with the COR-1 observations, and the LASCO observations with the COR-2 observations, thus ensuring a three–vantage point tracking throughout. The novelty of this work also lies in the fact that despite the unavailability of STEREO-B observations after 2016, we can still perform stereoscopy in the inner corona by combining data from COR-1A and K-Cor with the

help of this extended GCS model. In the following steps, we outline the fitting procedure carried out in this work.

Step 1. A pair of COR-1 images and a K-Cor image (taken at almost the same time) are selected, where the CME front is well developed in all three images.

S*tep 2*. The fitting procedure is then followed, as outlined in Thernisien et al. (2009) and Majumdar et al. (2020).

Step 3. The above two steps are repeated for the successive images in which the CME front is well developed in both the K-Cor and COR-1 FOVs.

Step 4. Since the time of the appearance of the CME in the K-Cor FOV might be different than that in the COR-1 FOV, a K-Cor image is then selected in which the CME front is first observed. Since three–vantage point observations are not available for this height, some of the model parameters are fixed, while the height, half-angle, and aspect ratio are readjusted as the model is fitted to the K-Cor images.

Step 5. Finally, the model is fitted to LASCO and the pair of COR-2 images to capture the evolution in the outer corona. The uncertainty in the fitting is determined in a similar way as mentioned in Thernisien et al. (2009) and Majumdar et al. (2020).

Examples of the GCS fitting to K-Cor and COR-1 images are shown in Figure 1, and a summary of the fitted parameters is given in Table 1. Panels (g) and (h) of Figure 1 further reflect the significance of this extended GCS model for the study of 3D kinematics in the inner corona, despite the unavailability of COR-1B data.

3. Results

3.1. Improvement in the Understanding of Early CME Kinematics

It should be noted here that, when selecting the events, although no preselection criterion was imposed for the CMEs to be impulsive, it turned out that all five of the CMEs studied showed the impulsive phase. In Figures 2(a) and (b), we plot the 3D kinematic profiles of the CMEs that occurred on 2014 June 14 and 2014 June 26. In the top panels, we plot the height–time data fitted with a cubic smooth spline (in red), followed by the speed and acceleration profiles (derived by taking the first- and second-order numerical derivatives of the height–time data) in the second and third panels, respectively. The overall fitting procedure and the estimation of the speed and acceleration are the same as reported in Majumdar et al. (2020). It should be noted here that the average uncertainty in the fitting of the GCS model was found to be 20%, and we did not find any appreciable change in latitude/longitude of these events beyond their uncertainties. However, it is worthwhile noting that a change in latitude/longitude will influence the height measurements, and hence for events that show considerable deflections, these considerations should be taken into account in future when estimating the uncertainty region in the absolute lower heights in the height–time profiles. We also plot the variation of the half-angle parameter (α) in the bottom panels. In the third panels, insets with zoomed-in plots of the residual acceleration phase are also provided in the bottom right-hand corners. Please note that the time axis of the zoomed-in insets overlaps with the common time axis shown at the bottom. We find that with the help of the observations from K-Cor, it is possible to capture the initial impulsive acceleration phase of the CMEs uniquely in the white-light data, thus eliminating the need to combine EUV observations with white-light observations for the capturing of the same, as was earlier reported in Bein et al. (2011; the initial gradual rise phase seems already to have been got over by the time that the CMEs reach the K-Cor FOV). It is worthwhile pointing out that this was not possible in Majumdar et al. (2020) or Cremades et al. (2020), as, for a number of events, the impulsive acceleration phase was already over by the time that the CME entered the COR-1 FOV, leading to an underestimation of the true acceleration, magnitude, and duration. Please note that in Figure 2, we show the kinematic profiles as representative examples of the two of the five impulsive CMEs studied, so as to demonstrate the capturing of the impulsive phase by using only white-light observations Further, as K-Cor offers a better cadence than COR-1 (in our case, we have used 2 minute cadence data), it helps with better tracking of the CME in the lower heights. Nonetheless, it must be noted that during the tracking of CMEs in the K-Cor and COR-1 overlapping FOV, the fitted times will be limited by the cadence of COR-1. In this regard, we would like to point out that although the K-Cor data offers a better cadence of 15 s, the CME fronts in the K-Cor data were fainter, and tracking the fronts was difficult. It should also be noted that sometimes the leading edge in the K-Cor image gets diluted in the higher heights of its FOV. Now, although this would introduce an uncertainty in the measured height, it is worth noting that the application of the GCS model leads to the tracking of a certain front of the CME (in this case, the leading front), and not a certain point on the leading front. Thus, in such cases, the other viewpoints from COR-1, where the CME leading front is better visible, helps in tracking the CME through those heights, while we use the K-Cor observations to track the CME at lower heights (as mentioned in Section 2.3), where the leading front is again better visible. The blue vertical dotted lines in the acceleration and half-angle evolution plots denote the time (and height) at which the impulsive acceleration ceases and the half-angle becomes constant, respectively. For the events studied, these heights happen to lie in the range of 2.5–3 $R_{\odot}$ (consistent with Cremades et al. 2020 and Majumdar et al. 2020).

3.2. Insights into the Width Expansion of CMEs

The use of three–vantage point observations helped in better constraining the GCS parameters (nevertheless, it should be noted that for the CME in 2016, only two vantage points were available, and for the heights below the COR-1 FOV, only K-Cor observations were used). Multiple–vantage point observations have shown that the width of a CME can be seen in two broad perspectives. CMEs tend to expand along the direction of their main axis, giving their axial width, and in the direction perpendicular to it, giving their lateral width (Cabello et al. 2016), which correspond to the face-on (FO) and edge-on (EO) CME widths, as presented in Thernisien et al. (2009). Thus, instead of just studying the evolution of the half-angle parameter as a proxy for studying the width expansion, we use the half-angle (α) and the aspect ratio (k) to calculate the FO and EO widths of the CMEs studied. This was possible once the GCS parameters for the CMEs were fixed by the three abovementioned vantage points, which were back-traced in the K-Cor FOV to heights of $\approx$1.1 $R_{\odot}$. From Table 1 of Thernisien (2011), the FO width (f_w) is related as

$$f_w = 2(\alpha + \mathrm{Sin}^{-1}k), \quad (1)$$

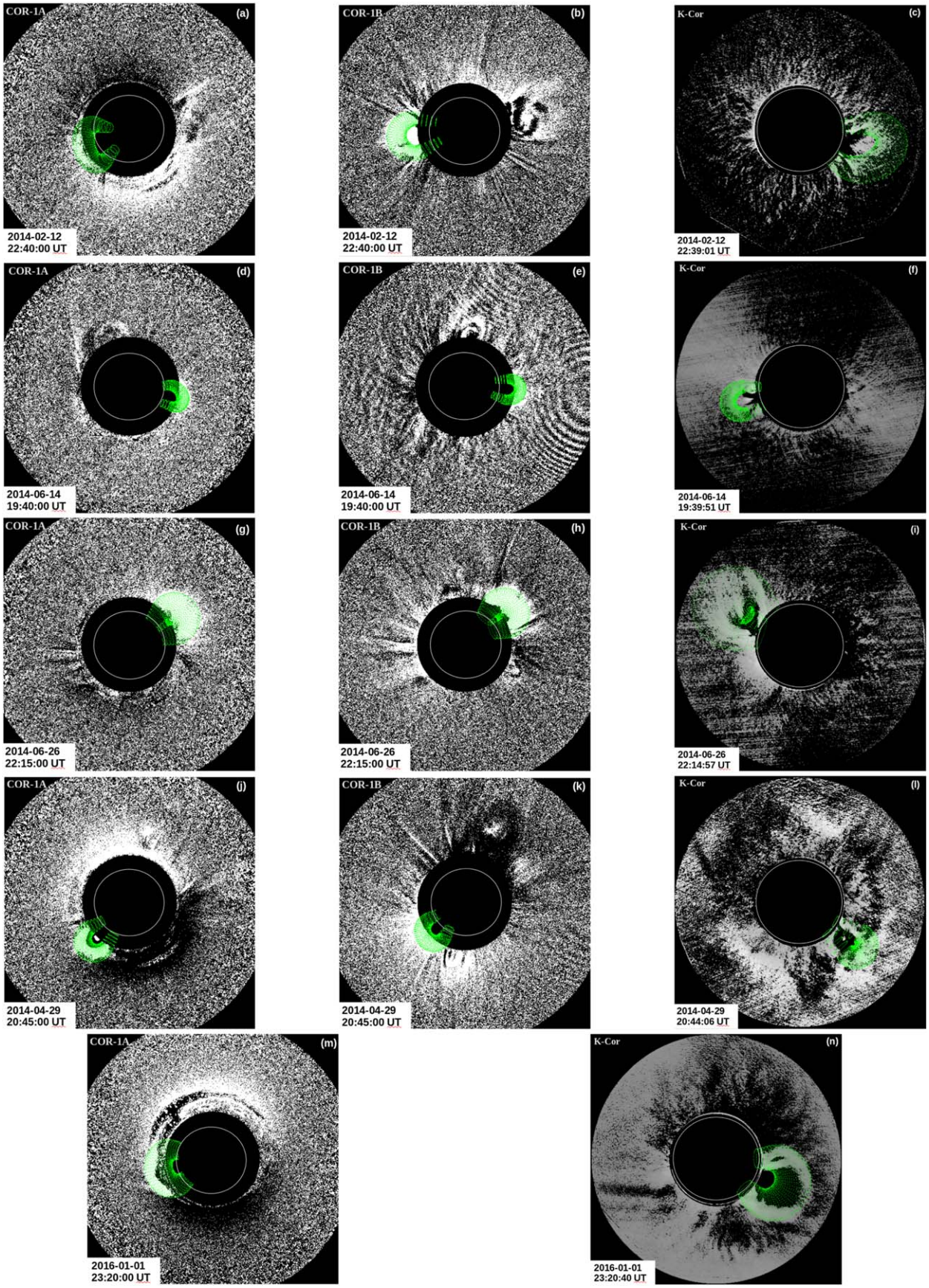

Figure 1. The fittings of the GCS flux rope to the K-Cor and pairs of COR-1 images for the five CMEs studied in this work.

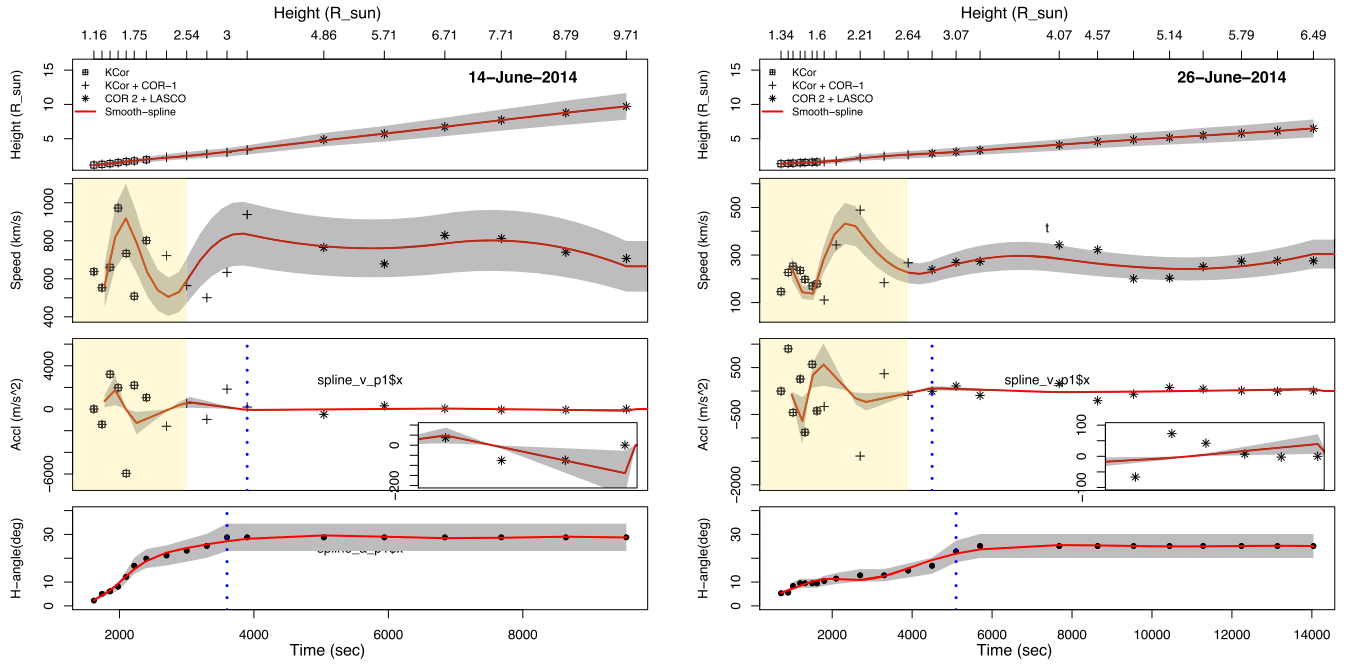

(a) CME on June 14 2014 (b) CME on June 26 2014

Figure 2. The complete 3D kinematic profiles of two of the five impulsive CMEs are shown as representative examples. The height–time data is fitted with a cubic smooth spline (shown in the solid red line). The speed and acceleration plots are obtained by taking first- and second-order numerical derivatives of the height–time plot. The gray shaded region corresponds to the uncertainty in the fitted model parameters. The impulsive phase is highlighted in yellow in the second and third panels. An insets with a zoom-in to the residual acceleration phase is provided in the bottom right-hand corner of the acceleration plot. Please note that the time axes of the zoomed-in insets overlaps with the common time axes shown at the bottom. In the bottom panel, the evolution of the half-angle (α) parameter is plotted.

Table 1
The GCS Model Parameters Fitted to the CMEs Are Tabulated

Date	Time (hh:mm:ss) (UT)	Longitude (ϕ) (deg)	Latitude (θ) (deg)	Tilt Angle (γ) (deg)	Height (h) ($R_\odot$)	Aspect Ratio (k)	Half-angle (α) (deg)
2014 Feb 12	22:40:00	102	−10	−45	2.79	0.16	24
2014 Jun 14	19:45:00	84	−13	64	2.29	0.14	23
2014 Jun 26	22:15:00	290	29	−68	2.86	0.36	13
2014 Apr 29	20:45:00	142	−39	−81	2.29	0.16	13
2016 Jan 1	23:20:00	330	−22	83	2.47	0.22	22

Note. The "Time" is the time of the observation; ϕ and θ are the longitude and latitude of the CME; the "Tilt Angle" (γ) is the angle between the axis of symmetry of the CME and the solar equator; h is the height of the leading front; the "Aspect Ratio" (k) is the ratio of the minor to the major CME radius; and α is the half-angle between the legs of the CME.

and the EO width (e_w) is related as

$$e_w = 2\,\mathrm{Sin}^{-1}k. \quad (2)$$

In Figures 3(a) and (b), we plot the variation of the FO and EO widths of the CMEs with height. We find that initially, until 3 $R_\odot$, both the FO and EO widths increase rapidly with height and then saturate, thus implying that at these lower heights, CMEs expand rapidly in both the axial and lateral directions. Similar behavior was also reported by Cremades et al. (2020), but it should be noted that they combined EUV and white-light observations to arrive at this conclusion, while our conclusions are based on using only white-light data uniquely. In this context, it is worthwhile noting that despite fitting the GCS model to three–vantage point observations, the estimations of the half-angle and aspect ratio can still have considerable uncertainties. One way to reduce such uncertainty is to use observations from instruments that are placed away from the ecliptic, as reported by Thernisien et al. (2009). So, in future, observations from the METIS (Fineschi et al. 2012) on board the Solar Orbiter (Müller et al. 2013) can be used to reach more precise estimations of these parameters. For the five CMEs, we found that the FO width starts in the range of 10°–30°, which then expands and becomes constant at 60°–90°. It should be noted that this was not possible in Majumdar et al. (2020), since only two vantage point observations were used (which is also the case for the fifth event in Table 1 in this work), which often leads to a degeneracy in the α and γ parameters (as reported in Thernisien et al. 2009; Majumdar et al. 2020), thus showing the importance of studying the true width of a CME, rather than the projected width, as the latter is highly dependent on the observer's line of sight (LOS). It must be noted that many of the earlier studies have ignored LOS effects on the CME width, and hence statistical studies of the width distribution (such as Pant et al. 2021, and references therein) can suffer from these projection effects.

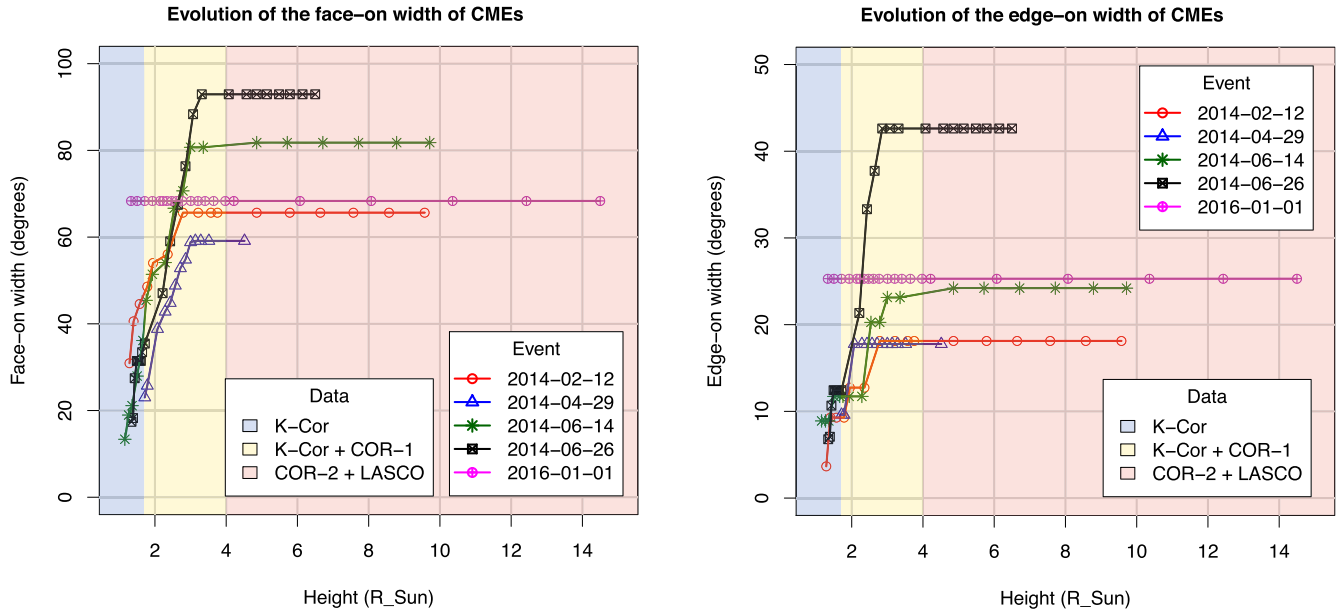

(a) Face-on width evolution (b) Edge-one width evolution

Figure 3. The evolution of the modeled (a) FO and (b) EO widths of the CMEs in the inner corona. Different regions of the plot are highlighted according to the data used.

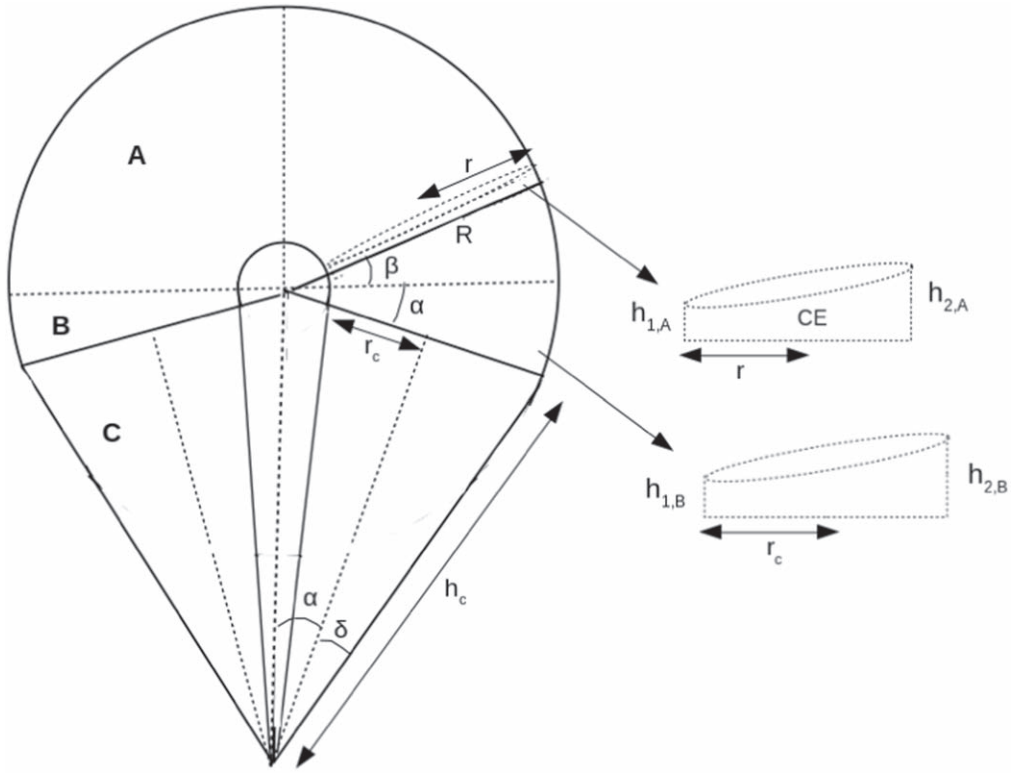

Figure 4. A schematic for the estimation of CME volume from the GCS-reconstructed 3D flux-rope structure. The entire CME volume can be subdivided into three parts—A: the ellipsoidal front; B: the asymmetric middle disk; and C: the conical legs. The figure is adapted from Holzknecht et al. (2018).

3.3. Evolution of the Modeled CME Volume

As reported by Holzknecht et al. (2018), the volume of a CME can be estimated from the GCS model, and it can be considered to be comprised of three parts: an ellipsoidal leading front (A in Figure 4), a middle asymmetric disk (B in Figure 4), and the conical legs (C in Figure 4). It should be noted here that all mathematical expressions are based on the work of Holzknecht et al. (2018). In order to calculate the volume of part A (V_A), it is assumed that the ellipsoidal front is made of very thin asymmetric cylindrical elements (CE in Figure 4). Now, the entire volume of A is covered with the angle β (see Figure 4), ranging from 0° to 90°. So we divide β into small

fractions γ, and thus each CE consists of a constant γ:

$$\gamma = \beta/n, \tag{3}$$

where n is the number of thin CEs. It should be noted that each of these CEs have two different heights, $h_{1,A}$ and $h_{2,A}$, where the second height is greater than the first height (see Figure 4, right panel). These heights are as follows:

$$h_{2,A} = R \tan(\gamma) \tag{4}$$

and

$$h_{1,A} = (R - 2r)\tan(\gamma). \tag{5}$$

Using these, the volume of each of these thin elements can be estimated as

$$V_{\rm CE} = \pi r^2 \left(\frac{h_{1,\rm A} + h_{2,\rm A}}{2}\right) = \pi r^2 (R - r)\tan(\gamma). \tag{6}$$

So, summing over all these elements, $V_{\rm A}$ is calculated as follows:

$$V_{\rm A} = \sum_{\gamma} \pi r^2 (R - r)\tan(\gamma). \tag{7}$$

Similarly, the volume of part B ($V_{\rm B}$) is calculated for a cylinder with different heights $h_{1,\rm B}$ and $h_{2,\rm B}$. From Figure 4, let

$$r|_{\beta} = 0 = r_0 \tag{8}$$

and

$$R|_{\beta} = 0 = R_0. \tag{9}$$

With these, we get the two heights of the cylinder as

$$h_{2,\rm B} = R_0\,\mathrm{Sin}(\alpha) \tag{10}$$

and

$$h_{1,\rm B} = (R_0 - 2r_0)\mathrm{Sin}(\alpha), \tag{11}$$

which gives the volume as

$$V_{\rm B} = \pi r_{\rm c}^2 \left(\frac{h_{1,\rm B} + h_{2,\rm B}}{2}\right) = \pi r_{\rm c}^2 (R_0 - r_0)\mathrm{Sin}(\alpha), \tag{12}$$

where r_c, from Figure 4 and from Thernisien (2011), is

$$r_{\rm c} = h_{\rm c}\,\mathrm{Sin}(\delta) = \mathrm{k}h_{\rm c}, \tag{13}$$

where h_c is the length of the conical legs. Finally, for the third part (C), which comprises the legs of the CME, it is simply the volume of the cone, which is the following:

$$V_{\rm C} = \frac{1}{3}\,\pi\, r_{\rm c}^2\, h_{\rm c}, \tag{14}$$

where, h_c, from Thernisien et al. (2009) and Thernisien (2011), is related to the GCS parameters as

$$h_{\rm front} = h_{\rm c}\,\frac{1}{1 - \mathrm{k}}\,\frac{1 + \sin(\alpha)}{\cos(\alpha)}. \tag{15}$$

Now, R and r are a function of the GCS model parameters k (aspect ratio), h (height), and α (half-angle), and can be found from Thernisien (2011). Since the model is axisymmetric, the total volume will thus be:

$$V_{\rm T} = 2(V_{\rm A} + V_{\rm B} + V_{\rm C}). \tag{16}$$

Thus, using the above three GCS model parameters, the modeled volume of the CME can be studied. A study of the GCS volume evolution was previously reported by Holzknecht et al. (2018), but they studied the volume evolution at the greater heights (15–215 $R_\odot$). Temmer et al. (2021) also used the GCS volume to study the CME density evolution with height in the outer corona (in the height range 15–30 $R_\odot$). But, in these studies, the crucial information of the volume evolution in the inner corona was missing. It should be noted that although CMEs are known to evolve self-similarly in the outer corona (see Subramanian et al. 2014), their propagation in the inner corona is non-self-similar (refer to Cremades et al. 2020; Majumdar et al. 2020). Thus, a study of the evolution of the modeled CME volume in the inner corona demands our attention. In this regard, although Temmer et al. (2021) used the GCS volume to estimate the densities of the magnetic ejecta and the sheath regions, an understanding of the volume evolution of the CME's leading front and the CME's legs has somehow evaded our understanding. With the incorporation of K-Cor observations with COR-1 for the GCS reconstruction, we now address these limitations in our understanding of CME volume evolution. Thus, we study the evolution of the modeled volumes of the CMEs in 3D in the inner and outer corona, separately for the different sections of the CME volumes (A—the ellipsoidal front, B—the asymmetric disk, and C—the conical legs, as shown in Figure 4).

In Figure 5, we plot the modeled total volume ($V_{\rm T}$; in black) evolution of the five CMEs with the distance from the Sun in panels (a), (b), (c), (d), and (e). We then fit a power law that reflects the dependence of the CME's volume on the distance from the Sun, as the CME propagates outward. This is the first time that any power-law relation has been reported for the evolution of modeled CME volumes with height. Also, since we have the separately estimated volumes for the ellipsoidal front, the middle asymmetric disk, and the conical legs of the CME, we study the evolution of these volumes as well and fit a power law to them for a better understanding. For instance, it is in the inner corona where the CME starts forming, and thus studying the volume evolution of the different parts of CMEs will enlighten us as to whether CMEs retain their shape as they propagate from the inner to the outer corona. Further, a study of the associated power-law profiles will help us to understand the scale-free behavior of the volume expansion of CMEs with height. In other words, a single power law for all the different parts of the CME volume would imply a single unified mechanism that drives the volume expansion of CMEs, while different power laws would imply a differential volume expansion, and hence the possibility of different driving mechanisms. In addition to that, if the mechanism of the acceleration and expansion of the CME (which in turn affects the volume) is the same in the inner and outer corona, then a single power law should be followed by the volume evolution profile in the inner and outer corona. However, if the power laws are different in the inner and outer corona, then that would imply that the mechanism of the increase in volume would probably be different in the inner and outer corona (as an outcome of the Lorentz force in the inner corona and the pressure difference in the outer corona). Thus, all these possibilities motivated us to probe the evolution of the modeled CME volumes in the inner and outer corona.

The details of the fitted power laws are given in Table 2. In order to appreciate the fitted empirical relations, we provide the associated R^2 values that show how well our model succeeds in determining the strength of the relationship between our model and the dependent variable on a 0–1 scale. We also provide the

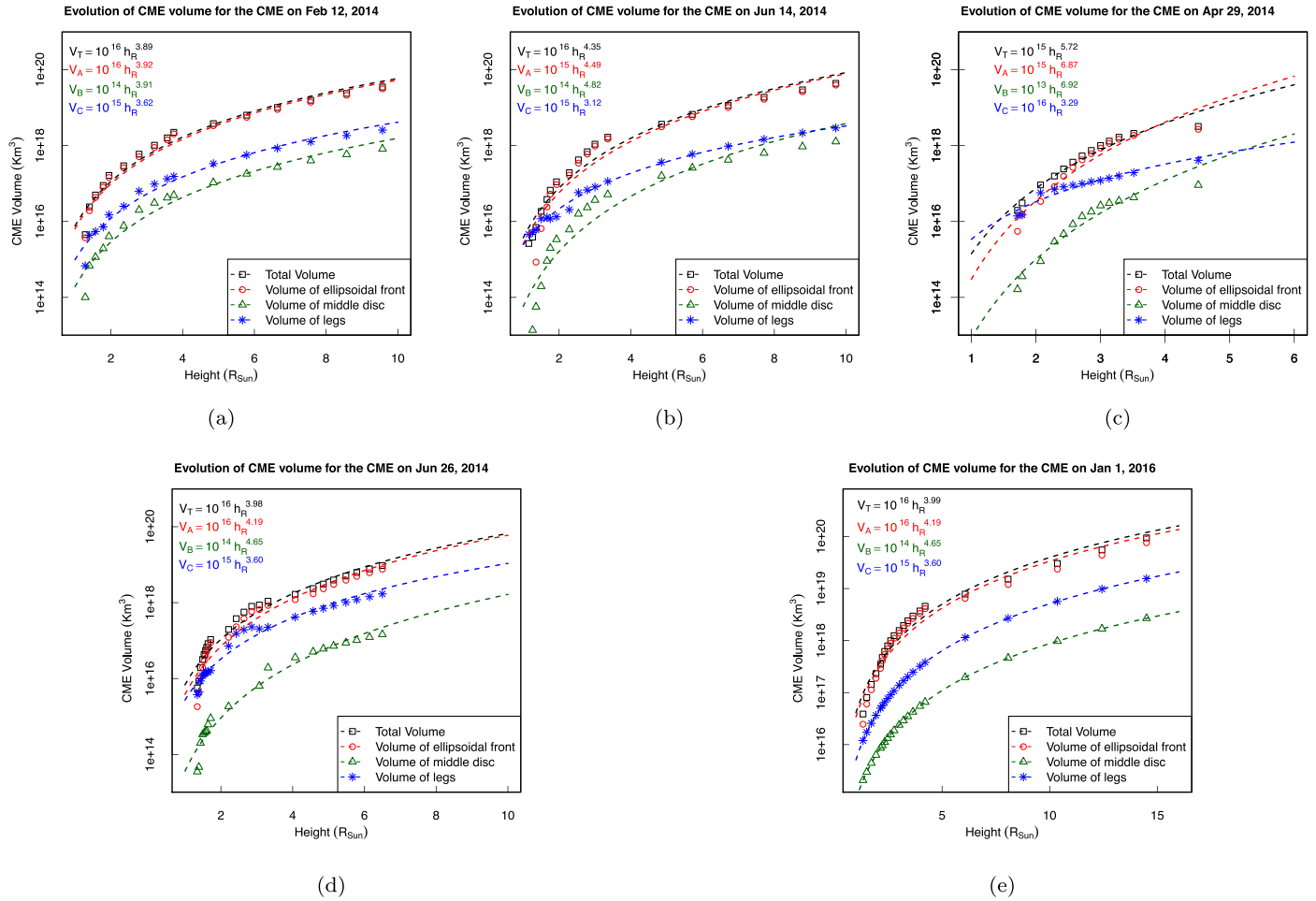

Figure 5. The evolution of the modeled CME volumes and their different parts. The color-coded plots denote the evolution of the different volume elements (the ellipsoidal front, the middle asymmetric disk, and the conical legs) in the inner and outer corona.

associated p-value, which shows the statistical significance of the fitted model. The average significance level was found to be 0.05 on average, and models with p-values less than 0.05 imply statistically significant results. We find that the power-law index for the total volume ranges between 3.89 and 5.72, thus indicating that the volume of a CME keeps increasing with the distance from the Sun within the investigated height. We further find that the volume of the leading ellipsoidal front (V_A) and that of the middle disk (V_B) varies with a higher power-law index (ranging between 3.92–6.87 and 3.91–6.92, respectively) than that of the total volume, while the volume of the conical legs (V_C) varies with a much lower power-law index (ranging between 3.12–3.62), thus indicating a differential volume evolution throughout a CME. This once again reflects the significance of studying both the FO and EO widths of CMEs. It is important to note that the volume of the legs of the CME is largely influenced by the EO width of the CME, while the volumes of the other two sections are influenced by both the FO and EO widths. However, it must also be kept in mind that the estimation of the volume of the legs by this method is only possible for CMEs with small aspect ratios (as is the case for the majority of the events studied; please see Table 1), which will enable the identification of two separate legs distinctly (as seen in the K-Cor images in Figure 1). For future studies of CMEs with large aspect ratios, it should be kept in mind that there will be a substantial overlap of the legs, and hence the estimation of the volume of the legs might be misleading in such cases.

From Figure 3, it can be seen that the EO widths are much less in magnitude as compared to the FO widths (which is an expected outcome of the geometry of the GCS model), and this is further reflected in the power laws as a slower increase in the volume of the legs of the CME as compared to the volumes of the ellipsoidal front and middle disk. We also note that the power law for the total volume is substantially greater for the CMEs on 2014 June 14 and 2014 April 29 as compared to the other three cases. We found that these two CMEs were ejected from erupting quiescent prominences, while the other three events were ejected from active regions. Recently, Pant et al. (2021) have reported a higher power-law index for the width distributions of CMEs connected to quiescent erupting prominences than those connected to active regions. It seems that the volume of a CME also shows a similar imprint of the source region, but our conclusion in this work is based on only five events, and hence an extension of this study to a much larger sample set of events will help to better establish our conclusions. In future, these results will also provide better inputs for studying the dynamics of mass accretion by CMEs as they evolve at the lower heights.

As discussed earlier, CMEs tend to evolve self-similarly in the outer corona, while the evolution in the inner corona is non-self-similar. This change in the behavior of the CMEs provoked

Table 2
The Empirical Relations for the Volume Evolution of the CMEs with the Corresponding R^2 Values and P-values for the Different Sections of the CMEs

Date	Volume Segment	Empirical Relation	R^2 Values	P-values
2014 Feb 12	Total (T)	$V_T = 10^{16}\ h_R^{3.89}$	0.96	1.5×10^{-11}
	A	$V_A = 10^{16}\ h_R^{3.92}$	0.96	2.0×10^{-11}
	B	$V_B = 10^{14}\ h_R^{3.91}$	0.96	4.7×10^{-11}
	C	$V_C = 10^{15}\ h_R^{3.62}$	0.97	2.9×10^{-12}
2014 Jun 14	Total (T)	$V_T = 10^{16}\ h_R^{4.35}$	0.96	8.3×10^{-13}
	A	$V_A = 10^{15}\ h_R^{4.49}$	0.92	5.1×10^{-9}
	B	$V_B = 10^{14}\ h_R^{4.82}$	0.91	4.1×10^{-9}
	C	$V_C = 10^{15}\ h_R^{3.12}$	0.99	2.2×10^{-16}
2014 Jun 26	Total (T)	$V_T = 10^{16}\ h_R^{3.98}$	0.95	2.3×10^{-15}
	A	$V_A = 10^{16}\ h_R^{4.19}$	0.93	1.9×10^{-13}
	B	$V_B = 10^{14}\ h_R^{4.65}$	0.96	2.7×10^{-14}
	C	$V_C = 10^{15}\ h_R^{3.60}$	0.96	2.2×10^{-16}
2014 Apr 29	Total (T)	$V_T = 10^{15}\ h_R^{5.72}$	0.95	1.2×10^{-8}
	A	$V_A = 10^{15}\ h_R^{6.87}$	0.93	1.0×10^{-7}
	B	$V_B = 10^{13}\ h_R^{6.92}$	0.94	7.3×10^{-8}
	C	$V_C = 10^{16}\ h_R^{3.29}$	0.93	1.2×10^{-7}
2016 Jan 1	Total (T)	$V_T = 10^{16}\ h_R^{3.99}$	0.96	2.8×10^{-15}
	A	$V_A = 10^{16}\ h_R^{4.19}$	0.95	9.3×10^{-14}
	B	$V_B = 10^{14}\ h_R^{4.65}$	0.99	2.2×10^{-16}
	C	$V_C = 10^{15}\ h_R^{3.60}$	0.99	2.2×10^{-16}

us to further study the total volume evolution of CMEs separately in the inner and outer corona. A close look at Figure 5 hints that the total volumes of the CMEs show different characteristics at different heights, and that a single power law is not able to fit the volume evolution for the entire height range. So, in Figure 6, we plot the evolution of the modeled total volume of the CMEs, and we fit two separate power-law profiles for the evolution of volume below and beyond 4 $R_\odot$ (please see Table 3 for the details of the fitting). It should be noted here that for the event on 2014 April 29, we could not track the CME much further in the COR-2 FOV, as the leading edge got depleted and was difficult to track. Thus, it was not possible to study the evolution of the modeled volume in the outer corona. We find that the volume evolutions for all the events follow different power-law profiles in the inner and outer corona. We find that the volume increases much more rapidly at the lower heights in the inner corona, as compared to the outer corona, thus clearly indicating the possibility of two different expansion mechanisms for CMEs at these two height regimes. The initial rapid expansion of the volume can be attributed to the rapid angular width expansion in the inner corona, as was recently reported by Cremades et al. (2020) and Majumdar et al. (2020), while it seems that the relatively slower volume expansion of CMEs in the outer corona might be a consequence of the total pressure difference in the inside and outside of the CME. These results thus strongly indicate how the kinematic properties of CMEs in the inner corona are strikingly different from the properties in the outer corona, lending support to the recent report by Majumdar et al. (2021b). It is also worthwhile noting the significance of the inclusion of the K-Cor data along with the COR-1 data in order to arrive at these results. The measurements in the K-Cor FOV have facilitated the distinct distinguishing of the contrast between the evolution of the modeled CME volume in the inner and the outer corona.

4. Discussions and Conclusions

We first present the feasibility of implementing GCS on the K-Cor data sets for the first time, thereby providing an additional vantage point for the 3D reconstruction of CMEs in the inner corona. A proof of concept of this application is presented in Figure 1, by fitting the GCS model to the near-simultaneous images of K-Cor along with the observations from the STEREO/SECCHI coronagraphs. The combined coronagraphic observations of K-Cor and STEREO/COR-1 in the inner corona and STEREO/COR-2 and SoHO/LASCO in the outer corona allowed us to track and study the true evolution of CMEs in white light, covering a FOV starting from as low as 1.1 $R_\odot$, which has not previously been achieved. This was possible once the GCS parameters for the CMEs were fixed by the three abovementioned vantage points, which were back-traced in the K-Cor FOV to heights of ≈1.1 $R_\odot$. This facilitated the capturing of the initial impulsive phase of the CMEs, where the kinematic parameters are known to change rapidly.

We were able to track the initial rapid expansions of the CMEs at these lower heights, and thanks to the three–vantage point observations, we found that the CMEs rapidly expand along both the axial and lateral directions in the initial part of the trajectory, until a height of 3 $R_\odot$, after which they saturate to a constant value. It should be noted here that only two vantage points were available for the CME in 2016, while only K-Cor observations were used for the heights below the COR-1 FOV. We noted that the CMEs can expand from ∼10° to more than 90° in FO width within the inner corona. For the sample of CMEs that we fitted, it could be identified that even though there was not much impulsiveness in the radial kinematics of the CMEs in the inner corona, we see a considerable expansion in their widths. An extension of this study on a larger data set will provide a better understanding of the Lorentz force in early kinematics of CMEs. In the future, an estimation of the true acceleration duration and magnitude can also be done at lower heights, without any underestimation of the mentioned quantities, which was not possible in Majumdar et al. (2020) and Cremades et al. (2020). It is worthwhile noting that we were able to do this using only white-light data (within the limitations of the GCS model), hence ensuring that any ambiguity arising from tracking a CME in EUV and white light is further evaded. Thus, this work will largely help in improving upon the shortcomings of previous studies of CME kinematics (Bein et al. 2011; Subramanian et al. 2014; Cremades et al. 2020; Majumdar et al. 2020). We further used the GCS model geometry to estimate the modeled total volume of the CME and also the separate modeled volumes of the ellipsoidal leading front, the asymmetric disk in the middle, and the conical legs. It should be noted that the correct estimation of the volumes of the different segments of the flux rope requires the unambiguous identification of the inner edge of the flux rope. But the identification of the inner edge of the flux rope is very difficult and tricky in the coronagraph images, and even if it is identified, it will suffer from high observer bias. However, provided that the FOV of the coronagraph provides

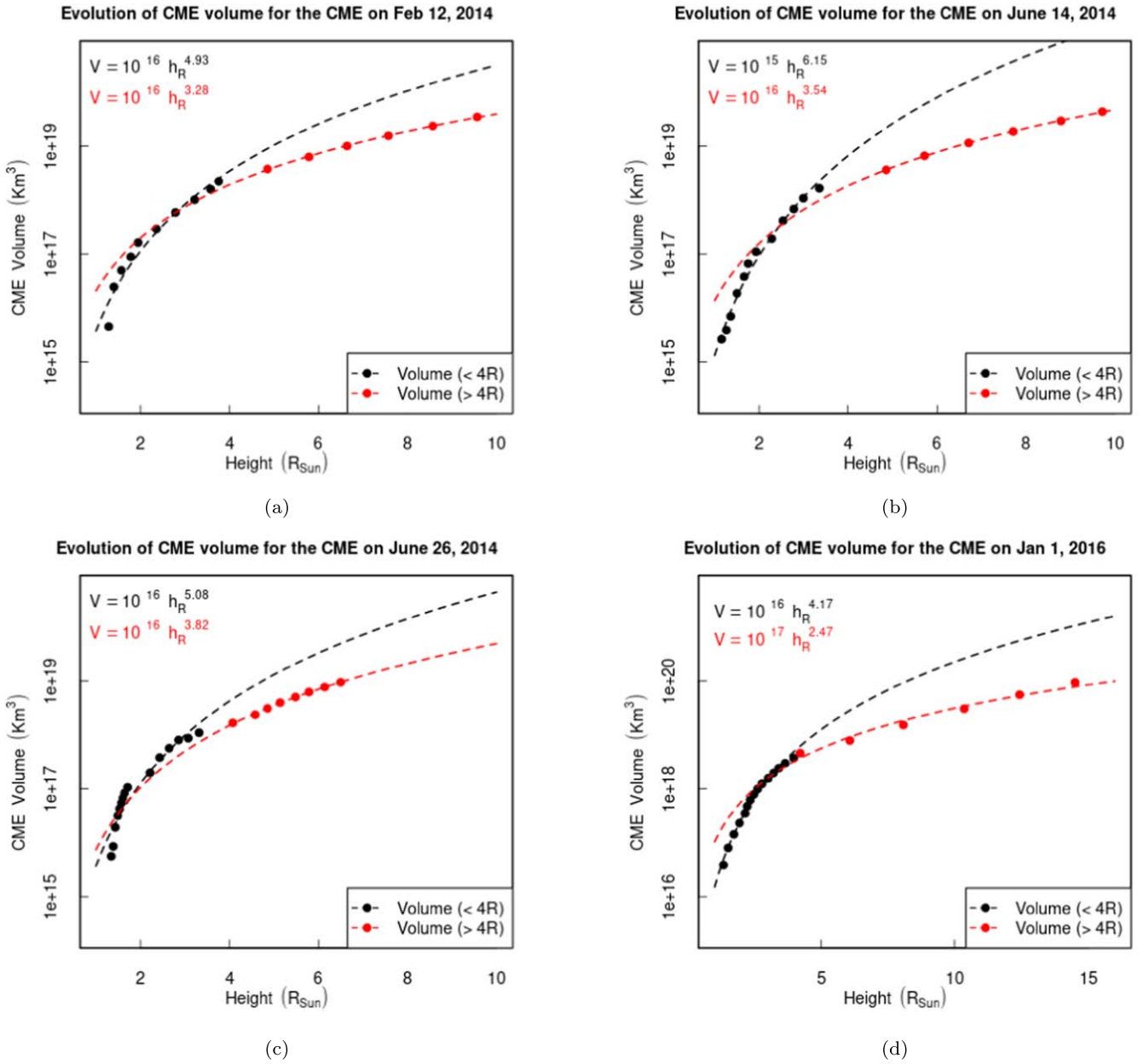

Figure 6. The evolution of the total modeled CME volumes in the inner and outer corona. The data points and curves in black mark the volume in the inner corona (<4 $R_{\odot}$), while the ones in red are for those in the outer corona (>4 $R_{\odot}$).

observations at the absolute lower heights to FO CMEs (as is the case for the K-Cor images in Figure 1), the inner edge of the flux rope can be identified and gauged at the CME legs. Here, in this context, all CMEs analyzed in this work are assumed to be oriented FO. We report for the first time a power-law variation of the modeled CME volume with distance from the Sun. We also found that the power law is higher for the ellipsoidal front and the disk than for the conical legs, thus indicating that the volume expansion is dominated by the former two parts, while the volume of the legs increases more slowly, thus indicating that there is a differential volume expansion through a CME as it propagates from the inner to the outer corona. In this context, it must also be kept in mind that the estimation of the volume of the legs using this method is only possible for CMEs with small aspect ratios (as it is in our case; please see Table 1), which will enable the identification of two separate legs distinctly (as seen in the K-Cor images in Figure 1). For future studies of CMEs with large aspect ratios, it should be kept in mind that there will be a substantial overlap of the legs, and hence the estimation of the volume of the legs might be misleading in such cases. We also studied the evolution of the modeled total volume of the CMEs in the inner and outer corona, and we found that CMEs tend to follow two distinctly different power-law profiles below and beyond 4 $R_{\odot}$. This hints at the possibility of two different expansion mechanisms of CMEs in the inner and outer corona. We believe that these results will need further attention in the future, which will help us to better understand the coupling of CME kinematics as they evolve from the inner to the outer corona. It is worthwhile noting that, as a consequence of the constraints of the fitting procedure at the absolute lower heights (as outlined in Section 2.3), the height measurements will be influenced for CMEs that get deflected at the lower heights. Now, although the CMEs studied in this work did not show any

Table 3
The Empirical Relations for the Volume Evolution of the CMEs in the Inner and Outer Corona with the Corresponding R^2 Values and P-values

Date	Region	Empirical Relation	R^2 Values	P-values
2014 Feb 12	$h_R < 4R_\odot$	$V = 10^{16}\ h_R^{4.93}$	0.95	1.5×10^{-6}
	$h_R > 4R_\odot$	$V = 10^{16}\ h_R^{3.28}$	0.99	2.3×10^{-7}
2014 Jun 14	$h_R < 4R_\odot$	$V = 10^{15}\ h_R^{6.15}$	0.98	1.5×10^{-10}
	$h_R > 4R_\odot$	$V = 10^{16}\ h_R^{3.54}$	0.99	2.5×10^{-8}
2014 Jun 26	$h_R < 4R_\odot$	$V = 10^{16}\ h_R^{5.08}$	0.91	2.4×10^{-8}
	$h_R > 4R_\odot$	$V = 10^{16}\ h_R^{3.82}$	0.99	3.1×10^{-9}
2014 Apr 29	$h_R < 4R_\odot$	$V = 10^{15}\ h_R^{5.72}$	0.95	1.2×10^{-8}
	$h_R > 4R_\odot$	...	...	...
2016 Jan 1	$h_R < 4R_\odot$	$V = 10^{16}\ h_R^{4.17}$	0.99	3.6×10^{-14}
	$h_R > 4R_\odot$	$V = 10^{17}\ h_R^{2.47}$	0.97	0.0002

appreciable deflection, such considerations should be kept in mind while studying CMEs that get deflected in the future, as this will increase the uncertainty in the height measurements. In addition to that, this work ignores the rotation of the CME at the lower heights, as no such observable evidence was noted. Now, despite the fact that no such observable signatures of deflections or rotations were noticed, it is worth noting that it is not that trivial to draw conclusions regarding these properties based solely on visual inspections. Hence, in the future, possibly with the inclusion of the above ecliptic data from METIS on board the Solar Orbiter, or observations from missions placed at the L5 point, we will be able to arrive at much stronger and better constrained conclusions. Thus, in the future, for CMEs that exhibit rotation, a change in the tilt angle parameter should also be considered when estimating the volume of the CME. Also, consideration of these processes (rotation and deflection) in future studies will also help in better understanding the evolution of the volumes of the CME's front and legs.

In this context, it must also be noted here that these conclusions are specific to the geometry of the GCS model, which is an idealized geometrical figure that has its limitations and constraints (see Thernisien et al. 2009). Regarding the evolution of the legs, the identification of the two separate legs of the CMEs requires observation at the absolute lower heights. Thus the legs can be identified in the K-Cor FOV, while they are not seen in the COR-1 FOV at the same time, as shown in Figure 1; but it should also be noted that despite the promising FOV of K-Cor, the poor image quality due to the challenges faced from it being a ground-based coronagraph makes it difficult to fit (refer to the discussion in Section 2.2). In this regard, the upcoming ADITYA-L1 mission (Seetha & Megala 2017), with the Visible Emission Line Coronagraph (VELC; FOV: 1.05–3 $R_\odot$; Banerjee et al. 2017; Prasad et al. 2017) on board, and PROBA-3 (FOV : 1.02–3 $R_\odot$; Renotte et al. 2014), with the giant Association de Satellites pour l'Imagerie et l'Interferométrie de la Couronne Solaire (ASPIICS; Lamy et al. 2017), will provide much better data and hence will help in arriving at much stronger conclusions on the evolution of CME legs. Having said that, it must also be noted that a true estimation of the volume of CME legs will require the CME to be seen FO, as an FO view will help in identifying the inner edges of the CME and hence the volume of its legs. The studied CMEs in this work are all seen FO in the K-Cor FOV (please see Figure 1). Thus, in future, for a larger statistical study, the appearance of the CME (whether FO or EO) should also be considered in the estimation of the volume of the CME legs. Apart from that, around one-third of CMEs have been reported as having a flux-rope morphology (see Vourlidas et al. 2013), which happens to be the bedrock of the GCS model, thus a study of the three separate sections of the flux-rope model of the CME will help us to have a much better understanding of the validity of self-similar expansion, and thus provide more precise constraints to models that study flux-rope initiation and evolution.

The cadence of K-Cor is better than that of COR-1, and this helped in tracking the CMEs more effectively at the lower heights, by capturing more data points in the impulsive phase. Since the speed and acceleration of a CME are obtained by taking first- and second-order derivatives of the height–time data, it is essential to have as many data points as possible, especially in the initial impulsive phase, so that the derived quantities are better estimated (Byrne et al. 2012). In this regard, although K-Cor provides a cadence of 15 s, the signal-to-noise ratio in that data is not good enough for confident tracking of the CMEs in most cases, which prompted us to use the 2 minute cadence data. Now, although this is a substantial improvement on the cadence of COR-1, it barely needs to be explained that data with an even better cadence will further aid our understanding of this initial rapid impulsive phase of CMEs. For this, again, the data from upcoming space missions like ADITYA-L1, with the VELC, and PROBA-3, with the ASPIICS, will help in overcoming this limitation, by providing high-cadence data with good resolution. The significance of this extension of the GCS model also lies in the fact that, despite the loss of the STEREO-B (and hence COR-1B data) from 2016, this modified GCS model will still enable stereoscopy in the inner corona for the 3D study of early kinematics of CMEs in white light.

We thank the anonymous referee for the valuable comments that have improved the manuscript. The authors acknowledge Dipankar Banerjee for his unstinting support and motivation throughout this project. The K-Cor data used in this work is courtesy of the Mauna Loa Solar Observatory, operated by the High Altitude Observatory, as part of the National Center for Atmospheric Research (NCAR). NCAR is supported by the National Science Foundation. The SECCHI data used here were produced by an international consortium of the Naval Research Laboratory (USA), Lockheed Martin Solar and Astrophysics Lab (USA), NASA Goddard Space Flight Center (USA), Rutherford Appleton Laboratory (UK), University of Birmingham (UK), Max-Planck-Institut for Solar System Research (Germany), Centre Spatiale de Liège (Belgium), Institut d'Optique Théorique et Appliquée (France), and Institut d'Astrophysique Spatiale (France). We also acknowledge the SoHO team for the LASCO data.

Facilities: K-Cor/MLSO, COR-1+COR-2/STEREO-A/B, LASCO/SOHO.

Software: IDL, R (R Core Team 2020).

ORCID iDs

Satabdwa Majumdar https://orcid.org/0000-0002-6553-3807
Ritesh Patel https://orcid.org/0000-0001-8504-2725
Vaibhav Pant https://orcid.org/0000-0002-6954-2276

References

Balmaceda, L. A., Vourlidas, A., Stenborg, G., & Dal Lago, A. 2018, ApJ, 863, 57
Banerjee, D., Patel, R., & Pant, V. 2017, in IAU Symp. 335, Space Weather of the Heliosphere, ed. C. Foullon & O. E. Malandraki (Cambridge: Cambridge Univ. Press), 340
Bein, B. M., Berkebile-Stoiser, S., Veronig, A. M., et al. 2011, ApJ, 738, 191
Brueckner, G. E., Howard, R. A., Koomen, M. J., et al. 1995, SoPh, 162, 357
Byrne, J. P., Morgan, H., Habbal, S. R., & Gallagher, P. T. 2012, ApJ, 752, 145
Cabello, I., Cremades, H., Balmaceda, L., & Dohmen, I. 2016, SoPh, 291, 1799
Cheng, X., Zhang, J., Kliem, B., et al. 2020, ApJ, 894, 85
Cremades, H., Iglesias, F. A., & Merenda, L. A. 2020, A&A, 635, A100
Fineschi, S., Antonucci, E., Naletto, G., et al. 2012, Proc. SPIE, 8443, 84433H
Gallagher, P. T., Lawrence, G. R., & Dennis, B. R. 2003, ApJL, 588, L53
Gopalswamy, N., Lara, A., Lepping, R. P., et al. 2000, GeoRL, 27, 145
Gosling, J. T. 1993, JGR, 98, 18937
Holzknecht, L., Temmer, M., Dumbović, M., et al. 2018, CEAB, 42, 3
Howard, R., Moses, J., Socker, D., Dere, K., & Cook, J. 2002, AdSpR, 29, 2017
Hundhausen, A. J., Sawyer, C. B., House, L., Illing, R. M. E., & Wagner, W. J. 1984, JGR, 89, 2639
Hutton, J., & Morgan, H. 2017, A&A, 599, A68
Joshi, A. D., & Srivastava, N. 2011, ApJ, 739, 8
Kaiser, M. L., Kucera, T. A., Davila, J. M., et al. 2008, SSRv, 136, 5
Kay, C., Opher, M., & Evans, R. M. 2015, ApJ, 805, 168
Lamy, P. L., Vivès, S., Curdt, W., et al. 2017, Proc. SPIE, 10565, 105650T
Majumdar, S., Paavan Tadepalli, S., Sankar Maity, S., et al. 2021a, SoPh, 296, 62
Majumdar, S., Pant, V., Patel, R., & Banerjee, D. 2020, ApJ, 899, 6
Majumdar, S., Patel, R., Pant, V., & Banerjee, D. 2021b, ApJ, 919, 115
Mierla, M., Davila, J., Thompson, W., et al. 2008, SoPh, 252, 385
Moore, R. L., Sterling, A. C., & Suess, S. T. 2007, ApJ, 668, 1221
Morgan, H., Byrne, J. P., & Habbal, S. R. 2012, ApJ, 752, 144
Morgan, H., Habbal, S. R., & Woo, R. 2006, SoPh, 236, 263
Müller, D., Marsden, R. G., St., Cyr, O. C., & Gilbert, H. R. 2013, SoPh, 285, 25
Pant, V., Majumdar, S., Patel, R., et al. 2021, FrASS, 8, 73
Patel, R., Pant, V., Iyer, P., et al. 2021, SoPh, 296, 31
Prasad, B., Banerjee, D., Singh, J., et al. 2017, CSci, 113, 613
R Core Team 2020, AR: A Language and Environment for Statistical Computing, R Foundation for Statistical Computing, Vienna, Austria, https://www.R-project.org/
Renotte, E., Baston, E. C., Bemporad, A. R., et al. 2014, Proc. SPIE, 9143, 91432M
Sachdeva, N., Subramanian, P., Colaninno, R., & Vourlidas, A. 2015, ApJ, 809, 158
Schwenn, R., dal Lago, A., Huttunen, R., & Gonzalez, W. D. 2005, AnGeo, 23, 1033
Seetha, S., & Megala, S. 2017, CSci, 113, 610
Song, H. Q., Zhang, J., Li, L. P., et al. 2019, ApJ, 887, 124
St. Cyr, O. C., Burkepile, J. T., Hundhausen, A. J., & Lecinski, A. R. 1999, JGR, 104, 12493
Subramanian, P., Arunbabu, K. P., Vourlidas, A., & Mauriya, A. 2014, ApJ, 790, 125
Suryanarayana, G. S. 2019, JASTP, 185, 1
Temmer, M., Veronig, A. M., Vršnak, B., et al. 2008, ApJL, 673, L95
Temmer, M., Holzknecht, L., Dumbović, M., et al. 2021, JGRA, 126, e28380
Thernisien, A. 2011, ApJS, 194, 33
Thernisien, A., Vourlidas, A., & Howard, R. A. 2009, SoPh, 256, 111
Thernisien, A. F. R., Howard, R. A., & Vourlidas, A. 2006, ApJ, 652, 763
Thompson, W. T., St., Cyr, O. C., Burkepile, J. T., & Posner, A. 2017, SpWea, 15, 1288
Vourlidas, A., Lynch, B. J., Howard, R. A., & Li, Y. 2013, SoPh, 284, 179
Vršnak, B., Maričić, D., Stanger, A. L., et al. 2007, SoPh, 241, 85
Webb, D., & Howard, T. 2012, LRSP, 9, 3
Zhang, J., & Dere, K. P. 2006, ApJ, 649, 1100
Zhang, J., Dere, K. P., Howard, R. A., Kundu, M. R., & White, S. M. 2001, ApJ, 559, 452
Zhang, J., Dere, K. P., Howard, R. A., & Vourlidas, A. 2004, ApJ, 604, 420
Zhao, X. H., Feng, X. S., Xiang, C. Q., et al. 2010, ApJ, 714, 1133